RSC Advances

PAPER

View Article Online
View Journal | View Issue

Cite this: *RSC Adv.*, 2024, **14**, 14784

Kill two birds with one stone: simultaneous removal of volatile organic compounds and ozone secondary pollution by a novel photocatalytic process†

Yifan Sui,[a] Xiaohu Sun,[a] Jie Guan,[a] Zeqiu Chen,*[a] Xinjie Zhu,[a] Xiaoyi Lou,[b] Xiuli Li,[a] Jiaowen Shen,[a] Xiaomei Liu,[c] Xiaojiao Zhang,[a] Yaoguang Guo,*[a] Gangfeng Zhang[d] and Rui-Qin Zhang[e]

Received 14th January 2024
Accepted 2nd May 2024

DOI: 10.1039/d4ra00366g

rsc.li/rsc-advances

Volatile organic compounds (VOCs) originating from diverse sources with complex compositions pose threats to both environmental safety and human health. Photocatalytic treatment of VOCs has garnered attention due to its high efficacy at room temperature. However, the intricate photochemical reaction generates ozone (O_3), causing secondary pollution. Herein, our work developed a novel "synergistic effect" system for photocatalytic co-treatment of VOCs and O_3 secondary pollution. Under the optimized reactor conditions simulated with computational fluid dynamics (CFD), MgO-loaded g-C_3N_4 composites (MgO/g-C_3N_4) were synthesized as efficient catalysts for the photocatalytic synergistic treatment process. Density functional theory (DFT) calculations, characterization, and electron paramagnetic resonance (EPR) tests revealed that the addition of MgO reduced the band gap of g-C_3N_4, and increased O_3 molecule adsorption in the composites, efficiently harnessing the synergistic effect of O_3 to generate a significant quantity of reactive oxygen radicals, thereby facilitating the removal of VOCs and O_3. This study provides new insights for simultaneous elimination of VOCs and O_3 secondary pollution by a photocatalytic process.

1. Introduction

In recent years, the emission of volatile organic pollutants (VOCs), precursors to fine particulate matter and photochemical smog, has surged significantly due to the extensive combustion of fuels, coupled with rapid industrial and transportation growth.[1,2] VOCs defined by the World Health Organization (WHO) as gaseous air pollutants with a boiling point of 50–260 °C, include acids, ketones, benzene, and nitrogen-containing, and oxygen-containing organics.[3,4] These compounds, known for their volatility, toxicity, and uncontrolled emissions, constitute a menace to the well-being of the general population.[5–8] For these rationales, the eradication of these pollutants is regarded as an imperative practical research subject. The main control strategies for VOCs generally consist of recovery methods such as condensation, absorption, and membrane separation.[9–11] Various elimination procedures, including catalytic combustion, low-temperature plasma, and biodegradation, are also utilized.[12–16] However, these methods frequently encounter disadvantages including the generation of additional contaminants, exorbitant expenses, heightened energy usage, and intricate operational protocols. Hence, there is a significant demand for the exploration of an efficient and straightforward method to eliminate VOCs under facile and mild conditions.

Photocatalytic technology, a component of the advanced oxidation processes (AOPs), stands out as a highly promising method for efficiently degrading VOCs under ambient conditions by generating reactive oxygen species (ROS), such as hydroxyl radicals ($^{\bullet}OH$) and superoxide radicals ($^{\bullet}O_2^-$), which possess strong oxidizing properties and facilitate the transformation of VOCs into carbon dioxide and water.[17–20] Nevertheless, the utilization of this technique is greatly limited by problems related to the non-properly designed reactor, deactivation of the catalyst and its low effectiveness. The commonly used 185 nm UV irradiation generates high-energy photons that commence the breakdown of oxygen and water, leading to the

[a]Shanghai Collaborative Innovation Centre for WEEE Recycling, School of Resources and Environmental Engineering, Shanghai Polytechnic University, Shanghai 201209, China. E-mail: zqchen@sspu.edu.cn; ygguo@sspu.edu.cn

[b]Laboratory of Quality Safety and Processing for Aquatic Product, East Sea Fisheries Research Institute, Chinese Academy of Fishery Sciences, Shanghai 200090, China

[c]School of Mathematics, Physics and Statistics, Shanghai Polytechnic University, Shanghai 201209, China

[d]Shanghai Academy of Environmental Sciences, Shanghai 200233, China

[e]Department of Physics, City University of Hong Kong, Hong Kong SAR, 999077, China

† Electronic supplementary information (ESI) available. See DOI: https://doi.org/10.1039/d4ra00366g

formation of reactive oxygen and ˙OH.[21–25] This process efficiently resolves the trade-off between efficiency and catalyst deactivation. However, the utilization of 185 nm UV irradiation in photocatalysis, is more prone to induce the production of ozone (O_3), potentially leading to secondary pollution.[26,27] Hence, it is imperative to tackle O_3 generation during 185 nm UV photocatalysis by implementing *in situ* catalytic or post-treatment measures.[28,29] Moreover, owing to its robust oxidizing capability, O_3 finds widespread application in the mitigation of diverse pollutants, encompassing wastewater treatment, exhaust gas purification, and microbial inactivation.[30–32] Consequently, the prospect of achieving synergistic removal of O_3 and VOCs through the utilization of *in situ* generated O_3 in the photocatalytic process is anticipated.

Developing appropriate photocatalysts is crucial for achieving the simultaneous elimination of VOCs and O_3 secondary pollution through synergistic processes. Due to its narrow band gap of 2.7 eV, appropriate redox potential, and strong stability, graphite-carbon nitride (g-C_3N_4) is extensively employed in the field of photocatalysis. Nevertheless, the limited surface area and rapid formation of photogenerated carrier complexes in pure g-C_3N_4 impede its broader use in photocatalysis.[33,34] Moreover, pure g-C_3N_4 cannot be directly utilized for the production of active substances from O_3. To tackle these issues, specialists have improved the application of g-C_3N_4 in photocatalysis by making changes to its shape and structure, incorporating different elements, and creating heterojunctions.[35,36] These enhancements aim to reduce the rate at which photogenerated carriers form complexes, thereby improving the practical use of g-C_3N_4. Muniandy *et al.* employed a catalyst consisting of copper-modified graphite carbon nitride nanosheets (Cu-g-C_3N_4) to successfully carry out the hydroxylation of benzene under mild conditions, utilizing H_2O_2 as an oxidizing agent.[37] Li *et al.* synthesized g-C_3N_4@Cs_xWO_3 nanocomposites that showed exceptional VOCs breakdown capabilities when exposed to a wide range of light wavelengths, including UV, visible, and near infrared ray (NIR).[38] Nevertheless, the previous researches have primarily concentrated on investigating the exceptional characteristics and reaction mechanisms of the created substances, while giving less attention to the possible ramifications of O_3 secondary pollution throughout the reaction procedure and its associated functions. Furthermore, multiple investigations have shown that the synergistic effect of combining the oxidizing and adsorbing properties of magnesium oxide (MgO) with O_3 leads to an enhanced conversion of O_3 into ˙OH, hence increasing the catalytic activity of O_3.[39] Agarkoti *et al.* employed the characteristics of MgO to expedite the breakdown of O_3, proved successful in treating CETP effluents.[40] MgO possesses favourable characteristics including strong surface reactivity, affordability, and environmental compatibility, rendering it a promising contender.[41]

Hence, this study explored a novel photocatalytic system with "synergistic effect" for co-treatment of VOCs and O_3 secondary pollution. Computational fluid dynamics (CFD) simulation tools were employed to model airflow rates and the distribution of UV lamp radiation within the photocatalytic reaction unit, offering a theoretical basis for rational reactor design. Exploiting the respective advantages of MgO and g-C_3N_4, the composite catalyst (MgO/g-C_3N_4) was synthesized, and subsequently fixed onto a cordierite carrier for the purpose of catalyzing the removal of toluene and *in situ* secondary generated O_3 at ambient temperature. Systematic adjustments of factors such as relative humidity, residence time, initial concentrations, and UV radiation were made to investigate optimal conditions. The reaction mechanism of the synergistic treatment of VOCs and O_3 using UV/MgO/g-C_3N_4 photocatalytic process was explored using material characterization tests, free radical determination, and density functional theory (DFT) calculations.

2. Experimental

Detailed information on materials, CFD simulation, catalysts synthesis, photocatalytic degradation processes, characterization and DFT calculation can be found in the ESI file.†

3. Results and discussion

3.1. Reactor optimization

To optimize the structure of the UV reactor, a more widely utilized model from existing engineering actual models was chosen for enhanced simulation. As shown in Fig. 1a, the airflow enters the chamber through the intake indentation in traditional equipment. While some of the airflow moves in the radial direction, it is mostly focused in the horizontal direction. Consequently, the airflow is not uniformly dispersed across the whole chamber. To solve this problem, a gas equalizer was introduced into the inlet indentation of the reactor (Fig. 1b) to disperse the gas flow at the entrance of the reaction system. This dispersion, facilitated by the gas equalizer, ensures a more even distribution of the gas flow within the reaction chamber. When viewed in a three-dimensions (Fig. 1c & d), the gas distribution

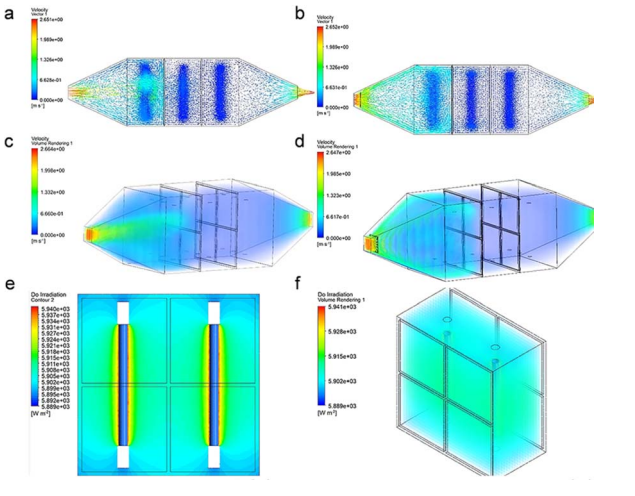

Fig. 1 Fluid trajectory of (a) conventional equipment and (b) improved equipment, spatial distribution of fluids in (c) conventional equipment and (d) improved equipment, (e and f) reactor radiation simulation.

is consistent with that described above. The inlet gas stream in the enhanced equipment exhibits a more uniform distribution within the chamber, leading to a reduction in the lateral velocity of the gas stream. This decrease in lateral flow velocity helps mitigate eddy currents around the catalyst carrier. To comprehend the dispersion of UV light within the chamber, an examination of the optical radiation emitted by the reactor was performed in a supplementary simulation. A part of it was intercepted for visualization to facilitate the analysis. The UV radiation is evenly distributed across the reaction chamber, as depicted in Fig. 1e & f, where the intensity of radiation from the UV lamp remains strong even at a certain distance from the UV lamp. Hence, the photocatalytic reactor possessing a gas equalizer was constructed to perform the following experiments. The model schematic and actual photos of the photoreactor (including the gas equalizer) are shown in Fig. S2.†

3.2. Catalyst characterizations

Morphologies of the samples were analyzed by scanning electron microscopy (SEM) and transmission electron microscopy (TEM). As shown in Fig. 2a and S3,† g-C_3N_4 exhibits a clear layered structure and is in the form of thin sheets. The pure MgO exhibits typical granular shape (Fig. 2b). From the SEM of 0.75MgO/g-C_3N_4, it can be seen that the MgO particles are loaded on the surface of g-C_3N_4 (Fig. 2c), ensuring the intimate electrical contact between MgO and g-C_3N_4. In addition, the TEM image of 0.75MgO/g-C_3N_4 (Fig. 2d) indicates that with the introduction of MgO, the basic structure of g-C_3N_4 remains unchanged and remains lamellar structure. In order to confirm the successful loading of MgO onto g-C_3N_4, the EDS characterization of the 0.75MgO/g-C_3N_4 was conducted, as depicted in Fig. 2f–i. The plots in Fig. 2h and i demonstrate the even distribution of O and Mg on the material surface, suggesting that MgO has effectively bonded with g-C_3N_4.

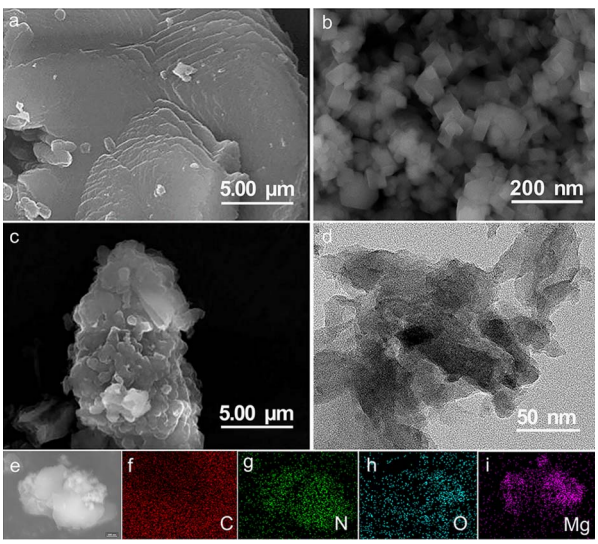

Fig. 2 SEM images of (a) g-C_3N_4, (b) MgO, (c) 0.75MgO/g-C_3N_4, (d) TEM images of 0.75MgO/g-C_3N_4, (e) EDS mapping positions and EDS elemental profiles (f) C, (g) N, (h) O and (i) Mg of 0.75MgO/g-C_3N_4.

X-ray diffraction (XRD) examination was conducted on MgO, g-C_3N_4, and MgO/g-C_3N_4 composites, as depicted in Fig. 3a. The g-C_3N_4 exhibits distinct peaks at 13.1° and 27.4°, corresponding to the (100) and (002) crystallographic planes, respectively. The presence of these peaks suggests that g-C_3N_4 exhibits planar interlayer stacking and a conjugated aromatic system, which aligns with the characteristics described in the standard card (JCPDS 87-1526) for g-C_3N_4.[42] The X-ray diffraction pattern of MgO has distinct peaks at 36.94°, 42.92°, and 62.30°, which correspond to the crystallographic planes (111), (200), and (220), respectively. All samples of MgO/g-C_3N_4 exhibit distinct diffraction peaks corresponding to both g-C_3N_4 and MgO, as shown in Fig. 3a. Furthermore, Fig. 3b displays the FTIR spectra of g-C_3N_4 and the composites of MgO/g-C_3N_4.

The FTIR spectra of g-C_3N_4 displays a distinct peak within the 1200–1650 cm^{-1} region. This peak corresponds to the characteristic stretching vibration of the C=N bond and the resonance of the C–N heterocycle.[43] The peak observed at 807 cm^{-1} is associated with the distinct vibrating of the triazine molecule. Furthermore, the spectral range of 3000–3400 cm^{-1} corresponds to a distinct peak in the N–H stretching vibration, which can be attributed to the existence of amino groups (–NH_2 or =NH) on the heptazine ring of g-C_3N_4.[44,45] The g-C_3N_4 exhibits a prominent peak within the 1200–1650 cm^{-1} range, which corresponds to the characteristic stretching vibration of the C=N bond and the vibration of the C–N heterocycle. The distinctive peaks of g-C_3N_4 and MgO/g-C_3N_4 composites exhibit a notable similarity. However, the peaks within the 1240–1640 cm^{-1} range are comparatively weaker in the composites

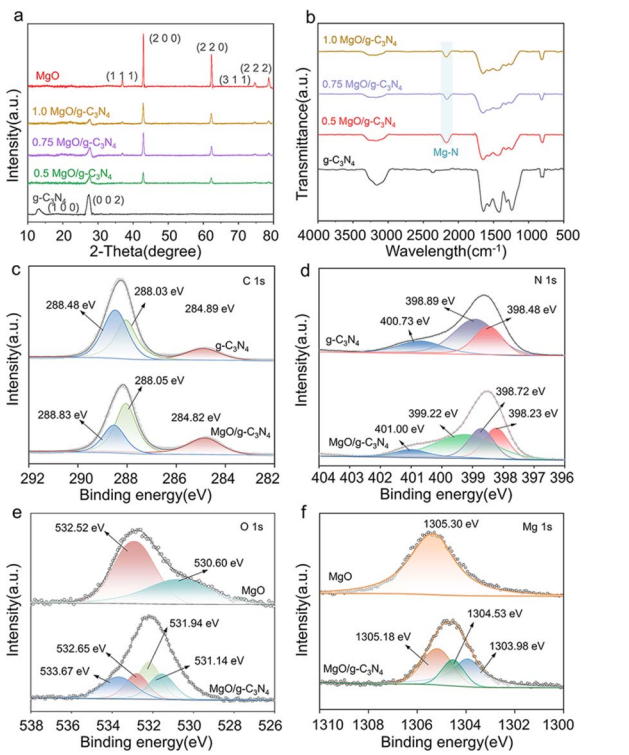

Fig. 3 (a) XRD pattern, (b) FTIR spectrum of the material, XPS patterns of (c) C 1s, (d) N 1s, (e) O 1s and (f) Mg 1s.

than those in g-C_3N_4. This observation can be attributed to the potential creation of a chemical link between Mg and N.[46] In addition, the newly observed signal at 2165 cm^{-1} corresponds to the vibration of the N–C–N bond, providing additional evidence for the presence of the Mg–N link between MgO and g-C_3N_4.[47] While the peak observed at 2360 cm^{-1}, which corresponds to the distinctive peak of C=N in pure g-C_3N_4, gradually diminishes with the addition of MgO, suggesting the production of Mg–N bonds.[48]

The XPS analysis was used to characterize the successful loading of MgO on g-C_3N_4. As illustrated in Fig. S4,† the presence of the Mg 1s peak at about 1304 eV and the enhanced intensity of the O 1s peak at roughly 530 eV in the complete spectrum of 0.75MgO/g-C_3N_4, as compared to that of g-C_3N_4, suggest the effective integration of MgO onto g-C_3N_4. The appearance of O 1s peaks on pure g-C_3N_4 can be attributed to the incorporation of oxygen during the calcination process.[49] The C 1s XPS spectrum (Fig. 3c) shows three different peaks detected at 284.82, 288.05 and 288.83 eV, corresponding to C–C, C–O and C–N bonds of MgO/g-C_3N_4, respectively.[50,51] The C–O and C–N bonds of MgO/g-C_3N_4 exhibit slightly higher binding energies than those of g-C_3N_4, which may be attributed to the electron-absorbing effect of MgO that alters the electronic environment of the C atoms in C–O and C–N. Fig. 3d displays three distinct peaks in the g-C_3N_4 material at energy levels of 398.48 eV, 398.89 eV, and 400.73 eV. These peaks correspond to the presence of sp^2 C–N=C, N–$(C)_3$, and C–N–H, respectively.[47] The newly observed signal at 399.22 eV in the MgO/g-C_3N_4 material can be attributed to the presence of the Mg–N bond.[52] In the high-resolution O 1s XPS spectrum of the MgO/g-C_3N_4 composite (Fig. 3e), a peak at 533.67 eV indicates the appearance of C–O coordination bonds. While, the peaks at 532.65 eV, 531.94 eV, and 531.14 eV correspond to adsorbed $^{\cdot}OH$, surface adsorbed H_2O, and the introduction of oxygen from air during calcination.[53] As shown in Fig. 3f, the high-resolution Mg 1s spectrum of MgO/g-C_3N_4 has two more peaks (1303.98 and 1304.53 eV) than that of pure MgO, which correspond to N–Mg–N and N–Mg–O bonds, respectively.[54] The negative shift of the peaks of Mg 1s and O 1s compared to pure MgO may be due to the charge transfer from g-C_3N_4 to MgO, reflecting the strong interaction between g-C_3N_4 and MgO.[49,55]

The UV-visible spectra of g-C_3N_4 and various series of MgO/g-C_3N_4 are presented in Fig. 4a. It is observed that MgO/g-C_3N_4 demonstrates a higher light absorption intensity compared to g-C_3N_4 in both the UV and visible regions. This suggests that the successful incorporation of MgO onto g-C_3N_4 enhances the efficiency of light absorption.[56] To study the change in band gap of the material before and after loading MgO, the band gap values of g-C_3N_4 and MgO/g-C_3N_4 materials were calculated based on the measured UV-vis plots. The band gap values of g-C_3N_4 and MgO/g-C_3N_4 materials were calculated in this study based on the measured UV-vis plots. Fig. 4b demonstrates a decrease in the band gap values of the materials upon the introduction of MgO to g-C_3N_4. This suggests that MgO/g-C_3N_4 produces a greater number of photogenerated carriers when exposed to light, thereby enhancing the catalytic efficiency.[57]

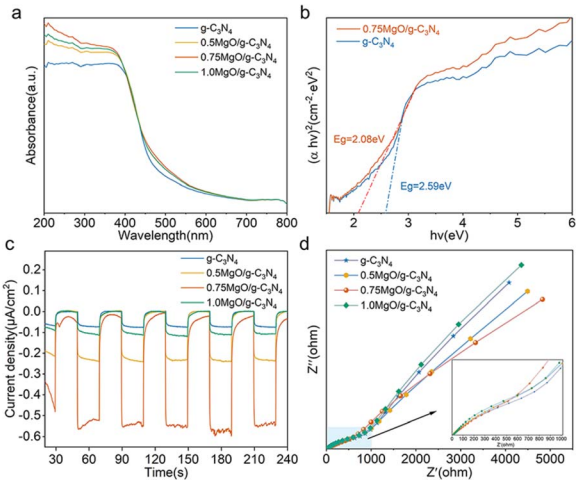

Fig. 4 (a) UV-diffuse reflectance spectra of the materials, (b) the band gap of g-C_3N_4 and 0.75MgO/g-C_3N_4, (c) photocurrent response diagram and (d) electrochemical impedance diagram of the material.

Fig. 4c demonstrates a notable enhancement in the photocurrent intensity of the MgO/g-C_3N_4 composites in comparison to that of g-C_3N_4. In particular, the 0.75 ratio of MgO/g-C_3N_4 has the strongest photocurrent response intensity. The correlation between higher photocurrent intensity and faster charge separation efficiency indicates that the presence of MgO enhances the charge separation efficiency of g-C_3N_4.[58] Electrochemical impedance analysis is commonly used to study the transfer of charge carriers at interfaces. As shown in Fig. 4d, the 0.75MgO/g-C_3N_4 material shows the smallest semicircle in all samples, which indicates that its interfacial charge carrier transfer is the fastest and more efficient for the separation and transport of photogenerated carriers.[59] In conclusion, the introduction of MgO can effectively reduce the band gap of g-C_3N_4, which is favourable for electron leaps and rearrangements. The formation of C–O and Mg–N bonds changes the electronic environments of C and N atoms in g-C_3N_4, which in turn promotes the transfer and separation of photogenerated carriers through Mg–N and C–O chemical bonds, which is expected to improve the photocatalytic performance of MgO/g-C_3N_4 in degrading pollutants.[60,61]

3.3. Catalytic performance

To investigate more comprehensively the degradation effect and the mechanism of synergistic effect in the MgO/g-C_3N_4/UV system, this study selected 0.75MgO/g-C_3N_4 with optimal optical properties as catalyst and investigated the optimal degradation conditions by controlling univariate variables. Firstly, the removal of toluene and O_3 by g-C_3N_4, MgO and MgO/g-C_3N_4 was compared under light conditions (Fig. S5†). The removal of toluene by MgO/g-C_3N_4 was significantly enhanced compared to g-C_3N_4 or MgO. In addition, the loading of MgO, which has excellent oxidation and adsorption properties with O_3, improved the O_3 removal ability of MgO/g-C_3N_4.[39,40] According to the data presented in Fig. S6a,† the rate of degradation reduces as the concentration increases. The

reaction system achieves its optimum efficiency at a concentration of 113.06 mg m^{-3}. This is mainly due to the fact that the capacity of the catalyst to treat pollutants per unit area is certain, and the degradation efficiency decreases due to the excessive number of pollutants not being degraded in time per unit time. Although lower concentrations of toluene exhibit higher degradation rates, higher concentrations favour O_3 elimination and utilization (Fig. S6b†). This is mostly attributed to the larger concentrations, which allow for greater contact between pollutants and O_3 on a per unit area and per unit time basis, thus the rate of O_3 removal is increased.[62]

Currently, many investigations indicate that the adsorption of organic pollutant molecules on the catalyst surface and the synthesis of active chemicals in the catalytic oxidation process are influenced by the relative humidity (RH) in the catalytic oxidation of VOCs, which has an impact on the degradation effect.[63–65] As shown in Fig. S6c,† the optimal toluene degradation rate occurs when the RH of the process system is approximately 60%; however, the toluene degradation efficiency decreases to a certain extent when the RH is too high or too low. This is mainly due to the fact that under high RH conditions, moisture in the gas stream will be adsorbed on the catalyst surface, which results in competitive adsorption with pollutant molecules,[66] while low RH will reduce the yield of active substances in the system, which will also reduce the degradation efficiency of toluene.[67] As shown in Fig. S6d,† there are also some differences in the synergistic elimination of O_3 under different RH conditions. This is possibly due to the fact that the presence of moisture in the reaction system affects the formation of reactive substances from O_3, which in turn affects the degradation of pollutants.[68]

The residence time determines the contact area and time of a certain amount of catalyst and pollutant per unit of time in the reaction system. Fig. 5a demonstrates that the degradation rate of the pollutants increases with decreasing inlet flow rate and toluene can be degraded with an efficiency of 95%. In addition, the concentration of O_3 is low under this condition and the removal rate is about 75% (Fig. 5b). This is possibly due to the fact that the slower flow rate allows greater contact between the pollutant and the catalyst in the reaction chamber, allowing the pollutant molecules to fully react with the active substances produced by the photocatalysis, resulting in a higher degradation efficiency of the pollutant. As shown in Fig. 5c, the decrease in the number of O_3-producing UV lamps results in a varying degree of reduction in the effectiveness of pollutant breakdown, and the concentration of terminal O_3 also decreases with the reduction of the generated amount. As shown in Fig. 5d, when the number of O_3-producing UV lamps is 3, the remaining O_3 concentration of the whole reaction system is nearly 0, which indicates that the system can effectively degrade organic pollutants and eliminate the secondary pollution brought by excess O_3 at the same time under the premise of certain O_3 concentration.

The system's versatility and cyclic stability were demonstrated by evaluating the degradation efficiency of ethyl acetate as well as long-term running and cycling experiments with toluene and ethyl acetate. As shown in Fig. 5e, the breakdown

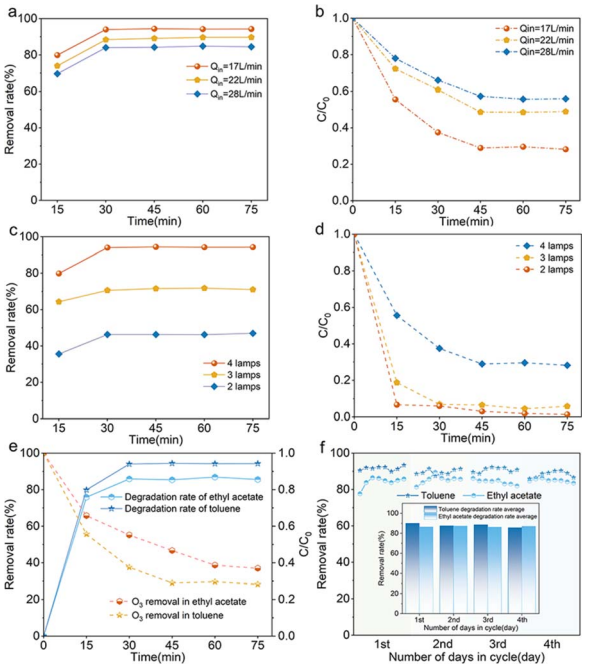

Fig. 5 Degradation of (a) toluene and (b) O_3 at different flow rates, degradation of (c) toluene and (d) O_3 at different radiation levels, (e) degradation efficiency of ethyl acetate and (f) degradation of toluene and ethyl acetate by catalyst recycling (inset shows the average degradation rate per cycle). Conditions: Q_{in} = 17 L min^{-1} except for (a and b), C_0 = 113.06 mg m^{-3}, RH = 61.2%.

rate of ethyl acetate in this system can exceed 85%, meeting regional emission standards (DB 31/933—2023). And the concentration of O_3 also decreases in this process, which indicates that this system still has a good degradation effect for other VOCs. As seen in Fig. 5f, the degradation rates of toluene and ethyl acetate were basically above 88% and 85% in each cycle, which indicated that the system could maintain a high degradation efficiency even under the long-time working conditions, and thus the reaction system had a good cyclic stability.

3.4. Mechanism discussion

With the successful introduction of MgO, the MgO/g-C_3N_4 forms Mg–N and C–O chemical bonds, and its band gap is smaller than that of pure g-C_3N_4, which improves the charge separation efficiency of g-C_3N_4, and enhances the separation and transport efficiency of photogenerated carriers. To further investigate the electronic behaviour and energy level changes upon loading, the energy band structure and density of states of g-C_3N_4 and MgO/g-C_3N_4 composites were analyzed by DFT calculations. The energy band structure and density of states for g-C_3N_4 and MgO/g-C_3N_4 are displayed in Fig. S7 and S8,† respectively, indicating that the energy band gap of the composites is significantly reduced due to the successful introduction of MgO. The density of states plot in Fig. S7† reveals that the energy band of g-C_3N_4 mostly comprises the s and p orbitals of C and N. Furthermore, the conduction band is

predominantly composed of the p orbitals of C and N. Compared to g-C_3N_4, the density of states plots of MgO/g-C_3N_4 in Fig. S8† shows an upward shift in the valence band energy and a downward shift in the conduction band energy, which results in a decrease in the band gap. Additionally, the s and p orbitals of the composite material contribute to both the valence and conduction bands. This indicates that the loading of MgO onto g-C_3N_4 facilitates the formation of band gap and more photogenerated carriers.[3]

To further investigate the synergistic mechanism of O_3 utilization by catalyst materials before and after MgO loading, the adsorption energy of catalysts for O_3, oxygen, and toluene was investigated in this paper. The change in adsorption energy of catalyst materials before and after MgO loading was calculated using DFT. The adsorption sites and adsorption energies of g-C_3N_4 and MgO/g-C_3N_4 on O_3, oxygen, and toluene are shown in Fig. 6. From the results, it is clear that the adsorption of O_3, O_2, and toluene is enhanced more obviously after the loading of MgO on g-C_3N_4, which indicates that the introduction of MgO is beneficial to the adsorption and utilization of O_3, O_2, and toluene. That is verified by adsorption experiments under light-free conditions (Fig. S9†), where the adsorption of toluene by MgO/g-C_3N_4 is about 20% higher than that of g-C_3N_4 in the first 30 min of the reaction, and the concentration of toluene tends to stabilize as the adsorption continues to be saturated. To further clarify the active compounds generated in the photocatalytic-O_3 synergistic system, auxiliary electron paramagnetic resonance (EPR) tests were conducted.[69] As shown in Fig. S10,† in the absence of light there is no production of active substances, in contrast, when the light is turned on a more pronounced $^{\cdot}OH$ (Fig. S10a†), $^{\cdot}O_2^-$ (Fig. S10b†) and $^1O_2$ (Fig. S10c†) signal peaks were produced. The addition of O_3 greatly amplified the signal peaks of the MgO/g-C_3N_4 system, suggesting the existence of a synergistic interaction between MgO/g-C_3N_4 and O_3.

Combining the characterization of materials, the detection of active substances during the reaction, the main active substances in the present system are $^{\cdot}OH$, $^{\cdot}O_2^-$ and $^1O_2$. In the present system, the dual role of MgO is crucial. Firstly, in the photocatalytic O_3 oxidation system, the chemical bond between MgO and g-C_3N_4 establishes the charge transfer channel, so MgO significantly speeds up the separation of photogenerated charges in g-C_3N_4 and boosts the production of $^{\cdot}OH$. In addition, MgO can improve the active site, increase the utilization of O_3, and actively decompose O_3, thus generating more $^{\cdot}OH$, which in turn creates an additional catalytic O_3 oxidation system. Therefore, there are three main ways to degrade pollutants in this system, as shown in Fig. 7: (I) a portion of the O_2 will undergo a direct reaction with electrons, resulting in the formation of $^{\cdot}O_2^-$. The generated $^{\cdot}O_2^-$ will then combine with H_2O to generate additional $^{\cdot}OH$, thereby intensifying the degradation of pollutants.[70] (II) O_2 is photolyzed in this system to produce O_3, and the photocatalytic material can be used to generate $^{\cdot}O_2^-$, which will further generate $^{\cdot}OH$ to degrade organic pollutants. The detailed process is as follows: high-energy UV light first cracks the oxygen molecules in the air to form (O(1D)) and triplet state oxygen atoms (O(3P)). Then, they react with oxygen molecules in the air to form O_3, and this reaction can be expressed by the eqn (1)–(3).[71] Subsequently, in the presence of ultraviolet light, the generated O_3 continues to form $O(^1D)$, which then reacts with water molecules in the air to form $^{\cdot}OH$, with the reaction eqn (4) and (5).[68] (III) The O_3 generated in the MgO/g-C_3N_4 synergistic system can be used as an electron trapping agent to accelerate the separation of photogenerated carriers should thus generate $^{\cdot}OH$, and eqn (6)–(8) demonstrate the generation process, while the generation of superoxide radicals and the final generation of $^{\cdot}OH$ can be expressed by eqn (9)–(12).[72,73] Due to the short lifespan of radical $^{\cdot}OH$ radicals, the generated radical $^{\cdot}OH$ radicals would transform into $^1O_2$ on the MgO/g-C_3N_4 surface by the disproportionation reaction (eqn (13)).[74]

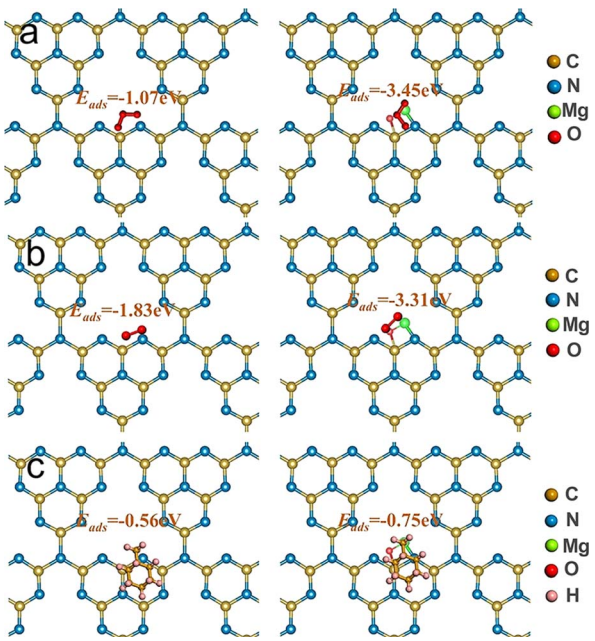

Fig. 6 Adsorption sites of (a) O_3, (b) O_2 and (c) toluene.

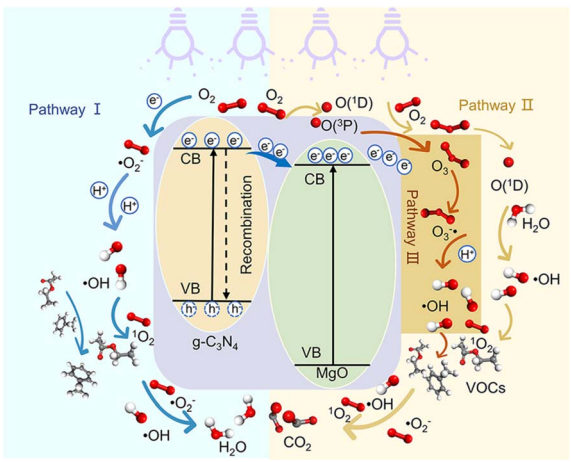

Fig. 7 Degradation mechanism diagram.

$$O_2 + h\nu(<243\ \text{nm}) \rightarrow O(^1D) + O(^3P) \quad (1)$$

$$O(^1D) + M \rightarrow O(^3P) + M\ (M = O_2 \text{ or } N_2) \quad (2)$$

$$O(^3P) + O_2 + M \rightarrow O_3 + M \quad (3)$$

$$O_3 + h\nu(<310\ \text{nm}) \rightarrow O(^1D) + O_2 \quad (4)$$

$$O(^1D) + H_2O \rightarrow 2^{\cdot}OH \quad (5)$$

$$h\nu(185\ \text{nm}) + H_2O \rightarrow {}^{\cdot}OH + H^+ \quad (6)$$

$$O_3 + e^- \rightarrow O_3^{-\cdot} \quad (7)$$

$$O_3^{-\cdot} + H^+ \rightarrow HO_3^{\cdot} \rightarrow O_2 + {}^{\bullet}OH \quad (8)$$

$$e^- + O_2 \rightarrow {}^{\cdot}O_2^- \quad (9)$$

$${}^{\bullet}O_2^- + H^+ \rightarrow HO_2^{\cdot} \quad (10)$$

$$HO_2^{\cdot} + H^+ + e^- \rightarrow H_2O_2 \quad (11)$$

$$H_2O_2 + e^- \rightarrow {}^{\cdot}OH + OH \quad (12)$$

$${}^{\cdot}OH + {}^{\cdot}OH \rightarrow {}^1O_2 + H_2O \quad (13)$$

To insight the degradation products of gaseous toluene, the gas chromatography-mass spectrometry (GC-MS) is often used to analyse the composition of the treated gas. In addition, *in situ* diffuse reflectance infrared Fourier transform spectroscopy (DRIFTS) allows the analysis of adsorbed substances on the catalyst during the reaction process, ultimately revealing the degradation intermediates.[75,76] Due to the limitations of the photoreactor, the study used GC-MS to explore the degradation products of toluene. As shown in Fig. S11,† the main intermediates in the photocatalytic degradation of toluene are the long-chain products produced by the ring-opening reaction, and a series of short-chain compounds such as alcohols, aldehydes, ketones, olefins, and so on, formed by further degradation.[77–79] Finally, these short-chain products were degraded to CO_2 and H_2O.

4. Conclusion

A novel photocatalytic system holding "kills two birds with one stone" was explored, *i.e.* towards simultaneous elimination of VOCs and O_3 secondary pollution. The distribution of airflow field and UV lamp radiation in the photocatalytic reaction device was simulated by CFD, which optimized the reactor design in this system. MgO/g-C_3N_4 synthesized as efficient catalysts for the photocatalytic oxidation process exhibit satisfied removal efficiencies for VOCs and O_3 under optimized conditions, which meets the industrial emission standard. On the other hand, the long-term degradation experiments of toluene and ethyl acetate indicate that the system possesses good stability and wide applicability. Based on DFT calculations and EPR experiments, the reaction mechanism for the effective degradation of pollutants by MgO/g-C_3N_4 was elucidated. These results might provide a new insight for the application of photocatalytic technology to remove VOCs and O_3 pollution in the industry.

Author contributions

Yifan Sui: investigation, visualization, writing original draft. Xiaohu Sun: methodology, and formal analysis. Jie Guan: resources and funding acquisition. Zeqiu Chen: writing – review & editing, and supervision. Xinjie Zhu: methodology, and investigation. Xiaoyi Lou: resources, and investigation. Xiuli Li: methodology, and investigation. Jiaowen Shen: methodology. Xiaomei Liu: methodology, and investigation. Xiaojiao Zhang: methodology. Yaoguang Guo: funding acquisition, writing – review & editing, and supervision. Gangfeng Zhang: methodology, and investigation. Rui-Qin Zhang: methodology, resources, and investigation.

Conflicts of interest

There are no conflicts of interest to declare.

Acknowledgements

The present work was financially supported by Natural Science Foundation of China (52270129, 52070127 and 52370142), Shanghai Natural Science Foundation (20ZR1421100), Oriental Talent Youth Program, Shanghai Shuguang Program (23SG52), Guizhou Provincial Key Technology R&D Program (QKHZC(2024)153) and Fundamental Research Funds of Shanghai Polytechnic University (EGD24DS15). Dr Guo also thanks the financial support of Science and Technology Development Fund of Pudong New Area (PKJ2022-C07, and PKJ2022-C10).

References

1 Z. Zhang, H. Wang, D. Chen, Q. Li, P. Thai, D. Gong, Y. Li, C. Zhang, Y. Gu, L. Zhou, L. Morawska and B. Wang, *Sci. Total Environ.*, 2017, **584–585**, 1162–1174.
2 Q. Zhang, B. Yuan, M. Shao, X. Wang, S. Lu, K. Lu, M. Wang, L. Chen, C. C. Chang and S. C. Liu, *Atmos. Chem. Phys.*, 2014, **14**, 6089–6101.
3 X. Liu, J. Zheng, K. Peng, G. Qin, Y. Yang and Z. Huang, *J. Environ. Chem. Eng.*, 2022, **10**, 107390.
4 Y. Guo, M. Wen, G. Li and T. An, *Appl. Catal., B*, 2021, **281**, 119447.
5 S. Weon and W. Choi, *Environ. Sci. Technol.*, 2016, **50**, 2556–2563.
6 J. Lee, J. Jang, J. Kim and S.-H. Lim, *Chem. Eng. J.*, 2022, **430**, 132891.
7 Y.-W. Li and W.-L. Ma, *Chemosphere*, 2021, **280**, 130667.
8 E. Cetin, M. Odabasi and R. Seyfioglu, *Sci. Total Environ.*, 2003, **312**, 103–112.
9 K. Kante, M. Florent, A. Temirgaliyeva, B. Lesbayev and T. J. Bandosz, *Carbon*, 2019, **146**, 568–571.

10 G. Zheng, K. Wei, X. Kang, W. Fan, N. L. Ma, M. Verma, H. S. Ng and S. Ge, *Environ. Pollut.*, 2023, **336**, 122451.
11 B. Shen, S. Zhao, X. Yang, M. Carta, H. Zhou and W. Jin, *Sep. Purif. Technol.*, 2022, **280**, 119974.
12 H. Huang, Y. Xu, Q. Feng and D. Y. C. Leung, *Catal. Sci. Technol.*, 2015, **5**, 2649–2669.
13 M. S. Kamal, S. A. Razzak and M. M. Hossain, *Atmos. Environ.*, 2016, **140**, 117–134.
14 S. Rouhani and F. Taghipour, *Chem. Eng. Sci.*, 2023, **272**, 118617.
15 X. Wu, Y. Lin, Y. Wang, S. Wu and C. Yang, *Chem. Eng. J.*, 2023, **471**, 144420.
16 J. R. Silva, D. S. Ascensão and L. M. Castro, *Energy Rep.*, 2020, **6**, 250–255.
17 J. Sun, X. Yan, K. Lv, S. Sun, K. Deng and D. Du, *J. Mol. Catal. A: Chem.*, 2013, **367**, 31–37.
18 W. Dechapanya, A. Eusebi, Y. Kimura and D. T. Allen, *Environ. Sci. Technol.*, 2003, **37**, 3662–3670.
19 J. Li, W. Cui, P. Chen, X. a. Dong, Y. Chu, J. Sheng, Y. Zhang, Z. Wang and F. Dong, *Appl. Catal., B*, 2020, **260**, 118130.
20 A. H. Mamaghani, F. Haghighat and C.-S. Lee, *Appl. Catal., B*, 2017, **203**, 247–269.
21 J. Ji, Y. Xu, H. Huang, M. He, S. Liu, G. Liu, R. Xie, Q. Feng, Y. Shu, Y. Zhan, R. Fang, X. Ye and D. Y. C. Leung, *Chem. Eng. J.*, 2017, **327**, 490–499.
22 J. Kim, P. Zhang, J. Li, J. Wang and P. Fu, *Chem. Eng. J.*, 2014, **252**, 337–345.
23 M. Li, Z. Qiang, P. Hou, J. R. Bolton, J. Qu, P. Li and C. Wang, *Environ. Sci. Technol.*, 2016, **50**, 5849–5856.
24 J. Jeong, K. Sekiguchi and K. Sakamoto, *Chemosphere*, 2004, **57**, 663–671.
25 P. Fu, P. Zhang and J. Li, *Int. J. Photoenergy*, 2012, **2012**, 174862.
26 K. Zoschke, H. Börnick and E. Worch, *Water Res.*, 2014, **52**, 131–145.
27 H. Claus, *Photochem. Photobiol.*, 2021, **97**, 471–476.
28 Y. Liu and P. Zhang, *J. Phys. Chem. C*, 2017, **121**, 23488–23497.
29 J. Ji, Y. Fang, L. He and H. Huang, *Catal. Sci. Technol.*, 2019, **9**, 4036–4046.
30 S. Lim, J. L. Shi, U. von Gunten and D. L. McCurry, *Water Res.*, 2022, **213**, 118053.
31 L. Xiang, L. Zhang, J. Shao, F. Lin, Z. Wang, B. Yan and G. Chen, *J. Hazard. Mater.*, 2023, **441**, 129997.
32 L. Z. Deng, A. S. Mujumdar, Z. Pan, S. K. Vidyarthi, J. Xu, M. Zielinska and H. W. Xiao, *Crit. Rev. Food Sci. Nutr.*, 2020, **60**, 2481–2508.
33 L. Chen, M. A. Maigbay, M. Li and X. Qiu, *Adv. Powder Mater.*, 2023, **1**, 100150.
34 R. Cheng, J. Wen, J. Xia, L. Shen, M. Kang, L. Shi and X. Zheng, *Catal. Today*, 2022, **388–389**, 26–35.
35 F. Fu, J. Yang, H. Xu, Y. Li, S. Cao, K. Da, W. Chen and X. Fan, *Chem. Eng. Sci.*, 2023, **276**, 118793.
36 X. Li, Y. Huang, W. Ho, S. Han, P. Wang, S. Lee and Z. Zhang, *Appl. Catal., B*, 2023, **338**, 123048.
37 L. Muniandy, F. Adam, A. R. Mohamed, A. Iqbal and N. R. A. Rahman, *Appl. Surf. Sci.*, 2017, **398**, 43–55.
38 Y. Li, X. Wu, J. Li, K. Wang and G. Zhang, *Appl. Catal., B*, 2018, **229**, 218–226.
39 G. Moussavi, A. Yazdanbakhsh and M. Heidarizad, *J. Hazard. Mater.*, 2009, **171**, 907–913.
40 C. Agarkoti, P. R. Gogate and A. B. Pandit, *Sep. Purif. Technol.*, 2022, **284**, 120281.
41 L. Du, W. Gao, Z. Li, W. Jiao and Y. Liu, *Chem. Eng. Process.*, 2020, **155**, 108053.
42 W. An, L. Tian, J. Hu, L. Liu, W. Cui and Y. Liang, *Appl. Surf. Sci.*, 2020, **534**, 147518.
43 Q. Chen, S. Li, H. Xu, G. Wang, Y. Qu, P. Zhu and D. Wang, *Chin. J. Catal.*, 2020, **41**, 514–523.
44 Y. Liang, R. Shang, J. Lu, L. Liu, J. Hu and W. Cui, *ACS Appl. Mater. Interfaces*, 2018, **10**, 8758–8769.
45 C. Zhou, P. Xu, C. Lai, C. Zhang, G. Zeng, D. Huang, M. Cheng, L. Hu, W. Xiong, X. Wen, L. Qin, J. Yuan and W. Wang, *Chem. Eng. J.*, 2019, **359**, 186–196.
46 L. Ge, Z. Peng, W. Wang, F. Tan, X. Wang, B. Su, X. Qiao and P. K. Wong, *J. Mater. Chem. A*, 2018, **6**, 16421–16429.
47 P. Ramacharyulu, S. J. Abbas, S. R. Sahoo and S.-C. Ke, *Catal. Sci. Technol.*, 2018, **8**, 2825–2834.
48 J. Zhou, X. Ji, X. Zhou, J. Guo, J. Sun and Y. Liu, *Sep. Sci. Technol.*, 2019, **54**, 2817–2829.
49 N. Mao and J.-X. Jiang, *Appl. Surf. Sci.*, 2019, **476**, 144–150.
50 M. Zhu, S. Kim, L. Mao, M. Fujitsuka, J. Zhang, X. Wang and T. Majima, *J. Am. Chem. Soc.*, 2017, **139**, 13234–13242.
51 X. An, X. Xu, W. Guo, Z. Chen, Z. Miao, J. Yuan and Z. Wu, *J. Environ. Manage.*, 2023, **344**, 118489.
52 W. Gao, *Graphene Oxide: Reduction Recipes, Spectroscopy, and Applications*, 2015, pp. 61–95.
53 C. Wang, H. Fan, X. Ren, J. Ma, J. Fang and W. Wang, *ChemSusChem*, 2017, **11**, 700–708.
54 J. Sun, H. Wu, C. Fu, C. Zhang, Z. Hu and M. Zhou, *Appl. Catal., B*, 2024, **351**, 123976.
55 Z. Zhang, R. Ji, Q. Sun, J. He, D. Chen, N. Li, H. Li, A. Marcomini, Q. Xu and J. Lu, *Appl. Catal., B*, 2023, **324**, 122276.
56 W. He, L. Liu, T. Ma, H. Han, J. Zhu, Y. Liu, Z. Fang, Z. Yang and K. Guo, *Appl. Catal., B*, 2022, **306**, 121107.
57 W. Wang, Z. Zeng, G. Zeng, C. Zhang, R. Xiao, C. Zhou, W. Xiong, Y. Yang, L. Lei and Y. Liu, *Chem. Eng. J.*, 2019, **378**, 122132.
58 I. Khan, S. Ali, M. Mansha and A. Qurashi, *Ultrason. Sonochem.*, 2017, **36**, 386–392.
59 S. Baqi, B. Deng, Y. Guo and R.-Q. Zhang, *J. Phys. Chem. C*, 2021, **125**, 25207–25216.
60 E. Giamello, D. Murphy, E. Garrone and A. Zecchina, *Spectrochim. Acta, Part A*, 1993, **49**, 1323–1330.
61 Y.-j. Hao, B. Liu, L.-g. Tian, F.-t. Li, J. Ren, S.-j. Liu, Y. Liu, J. Zhao and X.-j. Wang, *ACS Appl. Mater. Interfaces*, 2017, **9**, 12687–12693.
62 B. M. da Costa Filho, G. V. Silva, R. A. Boaventura, M. M. Dias, J. C. Lopes and V. J. Vilar, *Sci. Total Environ.*, 2019, **687**, 1357–1368.
63 F. Almomani, R. Bhosale and M. Shawaqfah, *Chemosphere*, 2020, **255**, 126878.

64 T. Gopi, G. Swetha, S. C. Shekar, R. Krishna, C. Ramakrishna, B. Saini and P. Rao, *Arabian J. Chem.*, 2019, **12**, 4502–4513.
65 C. H. A. Tsang, K. Li, Y. Zeng, W. Zhao, T. Zhang, Y. Zhan, R. Xie, D. Y. Leung and H. Huang, *Environ. Int.*, 2019, **125**, 200–228.
66 H. Gu, J. Lan, Y. Liu, C. Ling, K. Wei, G. Zhan, F. Guo, F. Jia, Z. Ai and L. Zhang, *ACS Catal.*, 2022, **12**, 11272–11280.
67 R. Radhakrishnan and S. T. Oyama, *J. Catal.*, 2001, **199**, 282–290.
68 J. Xiao, Y. Xie, F. Nawaz, S. Jin, F. Duan, M. Li and H. Cao, *Appl. Catal., B*, 2016, **181**, 420–428.
69 L.-S. Zhang, X.-H. Jiang, Z.-A. Zhong, L. Tian, Q. Sun, Y.-T. Cui, X. Lu, J.-P. Zou and S.-L. Luo, *Angew. Chem.*, 2021, **133**, 21919–21923.
70 J. Lei, B. Chen, L. Zhou, N. Ding, Z. Cai, L. Wang, S.-I. In, C. Cui, Y. Zhou and Y. Liu, *Chem. Eng. J.*, 2020, **400**, 125902.
71 J. Jeong, K. Sekiguchi, W. Lee and K. Sakamoto, *J. Photochem. Photobiol., A*, 2005, **169**, 279–287.
72 J. Xiao, J. Rabeah, J. Yang, Y. Xie, H. Cao and A. Brückner, *ACS Catal.*, 2017, **7**, 6198–6206.
73 P. Chen, Y. Mu, Y. Chen, L. Tian, X.-H. Jiang, J.-P. Zou and S.-L. Luo, *Chemosphere*, 2022, **291**, 132817.
74 M. Tian, X. Ren, S. Ding, N. Fu, Y. Wei, Z. Yang and X. Yao, *Environ. Res.*, 2024, **243**, 117848.
75 Q. Cheng, Z. Wang, X. Wang, J. Li, Y. Li and G. Zhang, *Nano Res.*, 2023, **16**, 2133–2141.
76 S. Fan, S. Luo, Y. Wang, X. Yue, D. Zheng, Z. Zhang, X. Fu and W. Dai, *Sep. Purif. Technol.*, 2024, **336**, 126256.
77 J. Rao, X. Chen, X. Zheng and C. Du, *Atmos. Pollut. Res.*, 2023, **14**, 101854.
78 S. Cao, L. Wu, J. Li, Y. Li, K. Da, W. Chen, R. Xue, J. Yang and X. Fan, *J. Environ. Chem. Eng.*, 2024, **12**, 112321.
79 L. Guo, J. Zhang, X. Zhang, R. Wang, Y. Jia and H. Long, *Mol. Catal.*, 2023, **550**, 113603.